



# Tailoring single-atom FeN<sub>4</sub> moieties as a robust heterogeneous catalyst for high-performance electro-Fenton treatment of organic pollutants

Pan Xia<sup>a</sup>, Zhihong Ye<sup>a,\*</sup>, Lele Zhao<sup>b</sup>, Qian Xue<sup>c</sup>, Sonia Lanzalaco<sup>d</sup>, Qiang He<sup>a</sup>, Xueqiang Qi<sup>c</sup>, Ignasi Sirés<sup>b,\*</sup>

<sup>a</sup> Key Laboratory of Eco-environments in Three Gorges Reservoir Region, Ministry of Education, College of Environment and Ecology, Chongqing University, Chongqing 400045, China

<sup>b</sup> Laboratori d'Electroquímica dels Materials i del Medi Ambient, Departament de Ciència de Materials i Química Física, Secció de Química Física, Facultat de Química, Universitat de Barcelona, Martí i Franquès 1-11, 08028 Barcelona, Spain

<sup>c</sup> School of Chemistry & Chemical Engineering, Chongqing University of Technology, Chongqing 400054, China

<sup>d</sup> Departament d'Enginyeria Química and Barcelona Research Center in Multiscale Science and Engineering, EEBE, Universitat Politècnica de Catalunya, C/Eduard Maristany, 10-14, 08019 Barcelona, Spain

## ARTICLE INFO

### Keywords:

Advanced oxidation process  
Electro-Fenton  
Metal-organic framework  
Single-atom catalyst  
Water treatment

## ABSTRACT

An iron single-atom catalyst, composed of robust FeN<sub>4</sub> moieties anchored on a nitrogen-doped porous carbon matrix (Fe-SAC/NC), has been developed via a surfactant-coordinated metal-organic framework (MOF) approach for application in heterogeneous electro-Fenton (HEF) process. The cohesive interaction between the surfactant and MOF precursor enabled the formation of abundant and stable FeN<sub>4</sub> moieties. The Fe-SAC/NC-catalyzed HEF allowed the complete degradation of 2,4-dichlorophenol with low iron leaching (1.2 mg L<sup>-1</sup>), being superior to nanoparticle catalyst synthesized without surfactant. The experiments and density functional theory (DFT) calculations demonstrated the dominant role of single-atom FeN<sub>4</sub> sites to activate the electrogenerated H<sub>2</sub>O<sub>2</sub> yielding <sup>•</sup>OH. The dense FeN<sub>4</sub> moieties allowed harnessing the modulated electronic structure of the SAC to facilitate the electron transfer, whereas the adjacent pyrrolic N enhanced the adsorption of target organic pollutants. Moreover, the excellent catalysis, recyclability and viability of the Fe-SAC/NC were verified by successfully treating several organic pollutants even in urban wastewater.

## 1. Introduction

As a result of the booming demand for healthcare products (e.g., pharmaceuticals), crop protection products (e.g., pesticides) and a myriad of synthetic industrial goods, refractory organic micropollutants, some of which act as endocrine disrupting chemicals (EDCs), are frequently present in water bodies and eventually jeopardize living beings health and ecosystems [1–4]. In the last decade, the electro-Fenton (EF) process has been demonstrated to be highly effective and eco-friendly alike for the treatment of such pollutants in wastewater [5, 6]. The EF setups rely on the electrogeneration of H<sub>2</sub>O<sub>2</sub> at carbonaceous cathodes, which occurs with great faradaic efficiency from O<sub>2</sub> reduction reaction. This in-situ reaction allows minimizing the dangers, hazards and costs associated to industrial H<sub>2</sub>O<sub>2</sub> synthesis [7–9]. The accumulated H<sub>2</sub>O<sub>2</sub> is immediately decomposed in the presence of Fe(II) catalyst, yielding abundant active hydroxyl radicals (<sup>•</sup>OH) in the bulk solution

via Fenton's reaction [6]. Nonetheless, the large-scale application of homogeneous EF (i.e., process in which free iron ions are used as catalyst) is limited by the requirement of strict acidic pH and the gradual conversion of dissolved iron into precipitate (mud) [10,11]. Lately, a strategy based in the use of solid iron-rich materials as heterogeneous EF catalysts has gained momentum to minimize these disadvantages, although new concerns have emerged in parallel [12]. The polyatomic nature of the catalysts limits the exposure of iron active sites to H<sub>2</sub>O<sub>2</sub>, which must be adsorbed prior to activation, and the relatively poor electron transfer between the reactants (especially the restrained Fe (III)/Fe(II) redox cycling) is detrimental to the overall catalytic performance [6,13]. Furthermore, the progressive deactivation and/or loss of active iron sites affects the catalyst stability and durability, ending in nonviable materials in practice [14,15]. It is thus evident that progress in design of catalysts with well-balanced performance and stability is of major importance.

\* Corresponding authors.

E-mail addresses: [yezhihong@cqu.edu.cn](mailto:yezhihong@cqu.edu.cn) (Z. Ye), [i.sires@ub.edu](mailto:i.sires@ub.edu) (I. Sirés).

<https://doi.org/10.1016/j.apcatb.2022.122116>

Received 23 July 2022; Received in revised form 22 September 2022; Accepted 25 October 2022

Available online 27 October 2022

0926-3373/© 2022 The Authors. Published by Elsevier B.V. This is an open access article under the CC BY-NC-ND license (<http://creativecommons.org/licenses/by-nc-nd/4.0/>).

At present, the development of strong Fe-N ensembles embedded in carbon matrices (denoted as Fe-N-C) is considered to be a promising strategy for the improvement of activity, stability and reusability of the iron-based catalysts [16,17]. N-doping contributes to the modulation of charge distribution of  $sp^2$ -hybridized carbon framework and creates new defects [18,19]. The electron-rich N sites coordinate with Fe atoms to form the so-called  $FeN_x$  moieties [20], which exhibit fast electron transfer ability and are considered as the actual active centers in many catalytic processes [21,22]. Moreover, the strong binding between Fe and N atoms confers a greater stability to the metal active sites and hence, to the whole catalyst during the given process [23]. As an example, Hu et al. fabricated an iron-based catalyst with core-shell structure and abundant  $Fe_3C$  and  $FeN_x$  sites; in an HEF system, the  $Fe_3C$  sites played a key role for  $H_2O_2$  generation and  $FeN_x$  promoted the  $H_2O_2$  activation [13]. Other studies have revealed the role of various N-functionalities present in the catalysts during the treatment of organic pollutants by Fenton-based processes; pyrrolic N facilitates the adsorption of pollutants through  $\pi$ - $\pi$  and/or cation- $\pi$  interactions, whereas N-doping eases the electron transfer through both the external circuit and the carbon framework to enhance the Fe(III) reduction [8,9,24,25]. As a result, the electronic configuration of the  $\pi$ -conjugated ligands linked to  $FeN_4$  sites is relocated, which alters the rate-determining steps of the given reaction. In this regard,  $FeN_4$  sites have been proven superior as compared to other coordination geometries ( $FeN_1$ ,  $FeN_2$  and  $FeN_3$ ) [26]. Unfortunately, for most Fe-N-C catalysts synthesized via conventional pyrolysis routes, a large proportion of  $FeN_x$  moieties are hidden and inaccessible to the reactants during the EF process, and the lack of strategies to precisely modulate the coordination number in  $FeN_x$  moieties limits the overall activity.

Single-atom catalysts (SACs), with individual metal sites atomically dispersed on the substrate, constitute a new frontier in catalysis. They have shown superior catalytic performance as well as higher selectivity and stability in many research fields due to their outstanding characteristics: unsaturated coordination configurations, fully exposed active sites, strong metal-substrate interactions and quantum size effects [17, 27–29]. The application of Fe-SACs in advanced oxidation processes has become a very relevant topic, as can be deduced from recent works: Chen and co-workers prepared Fe-SAC anchored nitrogen-rich g- $C_3N_4$  nanotubes for peracetic acid activation by Fenton-like reaction [30]; Xiong and co-workers fabricated an Fe-SAC using  $Fe(phen)_3$  and SBA-15 as the precursors for peroxymonosulfate activation [31]; several authors reported the application of Fe-SACs in HEF, trying to tune the multi-electron oxygen reduction process to enable the  $O_2$ -to- $\cdot OH$  conversion [32–34]. Unfortunately, few studies address the rational design of dense single-atom  $FeN_4$  sites for water treatment by HEF process, and the synthesis of SACs still remains challenging due to the easy aggregation of metal atoms [35,36].

Metal-organic frameworks (MOFs), as ultraporous materials formed by the spatial assembly of metal nodes and organic linkers, are common precursors to fabricate Fe-SACs due to the large number of metal sites, ordered pores, large exposed surface and diverse chemistry that is offered upon small structural changes [12,37,38]. Additionally, nitrogen atoms from the organic linkers can promote the anchorage of the highly mobile iron atoms, giving rise to strong  $FeN_x$  configurations [37,39–41]. Despite this, the methodology still suffers from considerable aggregation of iron atoms because of the carbon loss at high temperature [42]. This article addresses, for the first time, the rational design of an Fe-SAC with robust  $FeN_4$  moieties (Fe-SAC/NC) by the pyrolysis of a surfactant-coordinated MOF, followed by the application to boost HEF treatment of organic micropollutants in both model solution and urban wastewater. The involved surfactant, cetyltrimethylammonium bromide (CTAB), was able to regulate the crystallization of the MOF precursor, coordinating with the surface metal sites to form a surfactant shell. During the pyrolysis, the CTAB layers were decomposed into an N-doped carbon shell, which acted as additional carbon and nitrogen source to stabilize the iron single-atom sites and mitigate their agglomeration.

Some density functional theory (DFT) calculations are also included in this study, trying to elucidate the role of the single-atom  $FeN_4$  sites.

## 2. Materials and methods

### 2.1. Catalysts synthesis

The synthesis route of Fe-SAC/NC is schematized in Fig. 1a. In brief, 1.00 g of CTAB, 2.38 g of  $Zn(NO_3)_2 \cdot 6 H_2O$  and 1.10 g of  $FeSO_4 \cdot 7 H_2O$  were dissolved in 50 mL methanol to form a clear solution. Then, 50 mL of methanol containing 3.63 g of 2-methylimidazole were added into the above mixture. After stirring for 30 min at 60 °C, the resulting precipitate was centrifuged, sequentially cleaned with ethanol for several times, and finally dried at 60 °C for 12 h. The resulting MOF was transferred into a tube furnace to be heated at 900 °C for 3 h under nitrogen atmosphere. The carbonization product was treated with 0.2 M HCl solution for 2 h at 50 °C, then cleaned with ethanol and dried overnight. The final catalyst is denoted as Fe-SAC/NC or Fe1/2Zn-1.0CTAB. The preparation of catalysts with different CTAB dosage (0, 0.1, 0.5 and 1.5 g) followed a similar procedure, and the obtained catalysts are denoted as Fe1/2Zn-0CTAB (the absence of surfactant gives rise to nanoparticle catalyst, Fe-NP/NC), Fe1/2Zn-0.1CTAB, Fe1/2Zn-0.5CTAB and Fe1/2Zn-1.5CTAB, respectively.

### 2.2. Evaluation of catalytic performance

The electrolytic assays were carried out in a single chamber glass cell that contained 160 mL of solution to be treated at room temperature. The cell was equipped with a gas-diffusion electrode (GDE, 3 cm<sup>2</sup>) as cathode, with air supplied at 1 L min<sup>-1</sup> for constant  $H_2O_2$  production on site, and a Ti|IrO<sub>2</sub>-based dimensionally stable plate (DSA, 3 cm<sup>2</sup>) or a boron-doped diamond thin film (Si|BDD, 3 cm<sup>2</sup>) as the anode. The gap between the anode and cathode was 1.0 cm. Constant current was applied using a DC power supply (IT6302 from ITECH, China). The EF treatments were performed after catalyst addition. Samples were obtained at selected times and immediately filtered with PTFE syringe filters (0.22  $\mu$ m) to remove particles. The degradation performance was evaluated by measuring the concentration of pollutants using reversed-phase high performance liquid chromatography (HPLC, SCIION6000, China), as described in Supplementary Material (SM).

### 2.3. Characterization and analytical procedures

Several techniques, including X-ray absorption near edge structure (XANES) and extended X-ray absorption fine structure (EXAFS), high-resolution transmission electron microscopy (HRTEM), X-ray photoelectron spectroscopy (XPS), X-ray diffraction (XRD), thermogravimetric analysis (TGA), Raman analysis and inductively coupled plasma (ICP) were employed to analyze the morphology, chemical and electronic structures, and other properties of the synthesized materials. The details are given in SM. The analytical methods for determination of pH,  $H_2O_2$  and dissolved iron concentrations, and total organic carbon (TOC) are also explained in SM.

### 2.4. Computational details

Structural modeling and DFT calculations were carried out employing the Materials Studio software package. The exchange-correlation interaction was described by generalized gradient approximation (GGA) with the Perdew-Burke-Ernzerhof (PBE) functional. The Brillouin zone was sampled by a Monkhorst-Pack  $2 \times 2 \times 1$  K-point grid. The lattice constants were calculated using lattice parameters of  $14.726 \text{ \AA} \times 12.7825 \text{ \AA} \times 15.000 \text{ \AA}$ . The vacuum slab was set up to 15  $\text{\AA}$ . The geometric optimization was terminated when the energy and force on each ion dropped below  $10^{-5}$  Ha ( $3 \times 10^{-4}$  eV) and  $0.002 \text{ Ha \AA}^{-1}$  ( $0.05 \text{ eV \AA}^{-1}$ ).

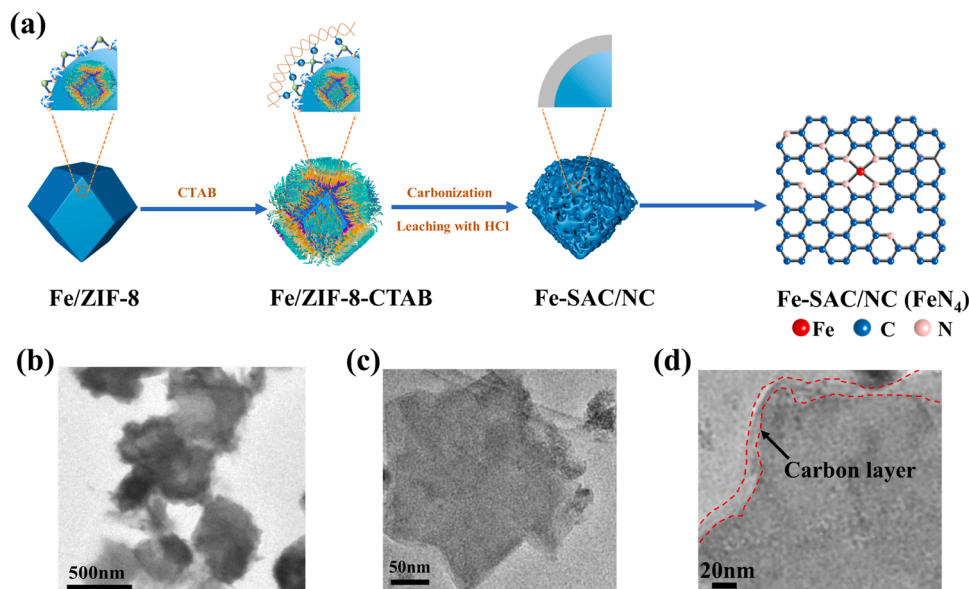


**Fig. 1.** (a) Scheme of the preparation method of the Fe-SAC/NC, ending in a representation of the atomic network. (b-d) TEM images of the obtained Fe-SAC/NC, at different magnifications.

### 3. Results and discussion

#### 3.1. Characterization of the MOF-derived catalyst

Fe-SAC/NC was prepared by carbonization of surfactant-coordinated Fe/ZIF-8 precursor at 900 °C under N<sub>2</sub> atmosphere (Fig. 1a). The surface Fe/Zn metal nodes in ZIF-8 crystals can coordinate with the hydrophilic groups of CTAB to form surfactant shells. The coordination-driven self-assembly slows down the crystal growth rate and controls the shape and

size of ZIF-8 crystals. During the pyrolysis, the surfactant layers were the first ones to decompose at temperature from around 330 °C (Fig. S1), forming ultrathin carbon layers at the surface. Finally, the zinc metal nodes were volatilized at high temperature (boiling point at 907 °C), leaving atomically-anchored Fe on the N-doped porous carbon matrices. Worth remarking, the cohesive interaction between CTAB and MOF crystals allowed a confinement effect that suppressed the agglomeration of Fe atoms, eventually yielding a large amount of atomically dispersed FeN<sub>4</sub> active sites. Moreover, the N groups in CTAB provide additional N

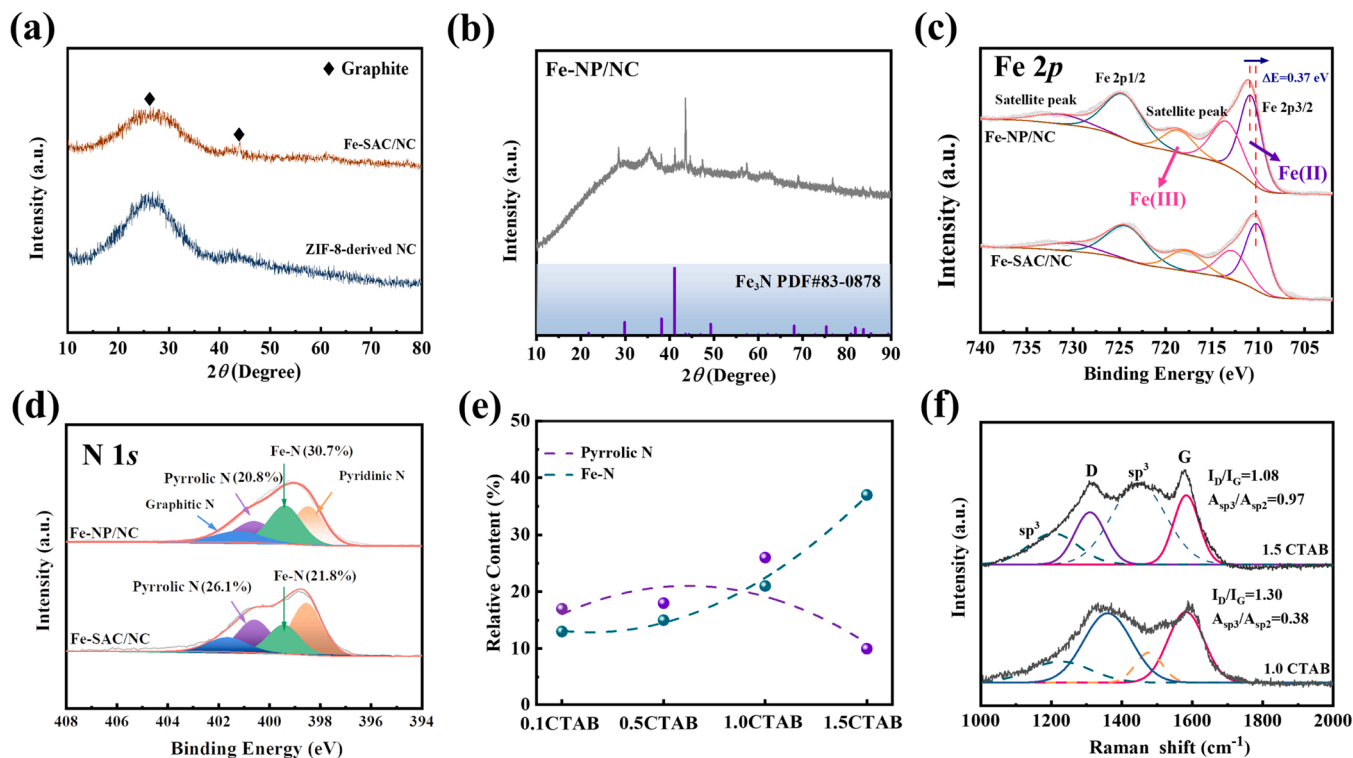


**Fig. 2.** XRD patterns of (a) Fe-SAC/NC and ZIF-8-derived NC and (b) Fe-NP/NC. High resolution (c) Fe 2p and (d) N 1s XPS spectra of Fe-NP/NC (prepared with 0 g CTAB) and Fe-SAC/NC (prepared with 1.0 g CTAB). (e) The pyrrolic N and Fe-N percentages in the catalysts with the CTAB content employed during the synthesis. (f) Raman spectra of Fe1/2Zn-1.0CTAB and Fe1/2Zn-1.5CTAB.

source to enhance the coordination between Fe and N [43]. The TEM images depicted in Fig. 1b-d also confirm the distinct carbon layer coating on the surface, and the catalyst partially inherited the morphology of the MOF precursor, which may enhance the stability and the mass transport during the reaction. The XRD patterns of Fe-SAC/NC and ZIF-8-derived N-doped carbon matrices, as shown in Fig. 2a, exhibited only two peaks centered at  $24.3^\circ$  and  $44.5^\circ$ , which were assigned to (002) and (004) crystal planes of carbon, respectively [44, 45]. No diffraction peak related to Fe-based species (iron oxides, iron nitrides or iron carbides) appeared, evidencing that Fe sites were atomically dispersed in Fe-SAC/NC. In contrast, a high amount of Fe atoms in the Fe-NP/NC, prepared in the absence of CTAB, existed in the diffractogram of  $\text{Fe}_3\text{N}$  (Fig. 2b) [46].

Further evaluation of the coordination state and electronic features of Fe-SAC/NC is crucial for in-depth understanding of the catalytic mechanisms underlying in the HEF system. First, the XPS analysis was performed to reveal the chemical compositions and the corresponding electronic states of the catalyst. The high resolution Fe 2p spectra of Fe-NP/NC and Fe-SAC/NC (Fig. 2c) illustrate two splitting peaks at binding energies of 710.8 and 713.4 eV for the former material, which could be attributed to Fe(II) and Fe(III) species, respectively [47,48]. However, both peaks in Fe-SAC/NC slightly shifted to lower binding positions (710.2 and 712.8 eV), whereas the peak area of Fe(II) increased to 63.3% compared to the 58.1% in Fe-NP/NC. These results are ascribed to the introduction of CTAB, which enhances the dispersion of Fe atoms and the formation of  $\text{FeN}_x$  moieties during the pyrolysis. Nitrogen from CTAB can bond with iron atoms and decrease their electron density, thus enhancing the Fe(III) to Fe(II) conversion by accelerating the electron transfer from carbon to iron sites [49,50]. Meanwhile, the increase in the amount of carbon in Fe-SAC/NC (Fig. S2) further facilitated the stabilization and reduction of Fe(III) atoms. Additionally, the Fe loading in Fe-SAC/NC was measured by ICP as 8.5 wt%. In N 1s spectra (Fig. 2d), graphitic N (401.3 eV), pyrrolic N (400.3 eV), Fe-N (399.7 eV), and pyridinic N (398.9 eV) were observed in both samples [21,51–54]. Worth noting, the proportion of pyrrolic N was higher and Fe-N was lower in Fe-SAC/NC as compared to Fe-NP/NC. As reported, Fe-N sites usually act as the catalytic centers for the activation of  $\text{H}_2\text{O}_2$  to form

$\cdot\text{OH}$ , and pyrrolic N can serve as adsorption sites for target pollutants during the wastewater treatment [13,55,56]. Therefore, higher amount of pyrrolic N and Fe-N may give rise to better catalytic performance of the catalysts. In addition, the proportion of pyrrolic N and Fe-N was greater with the increase of CTAB dosage during the synthesis, but excessive CTAB (i.e., 1.5 g) led to the decrease in the proportion of pyrrolic N (Fig. 2e).

Further analysis of the surface defect states of Fe1/2Zn-1.0CTAB and Fe1/2Zn-1.5CTAB was conducted by Raman spectroscopy. In Fig. 2f, two distinct peaks are observed at  $1350\text{ cm}^{-1}$  and  $1600\text{ cm}^{-1}$ , which are assigned to defective D and graphitic G bands, respectively. These two peaks can be further deconvoluted into four peaks through Gaussian numerical simulation, namely the  $\text{sp}^2$ -type (at  $\sim 1350\text{ cm}^{-1}$  and  $\sim 1600\text{ cm}^{-1}$ ) and the  $\text{sp}^3$ -type carbon (at  $\sim 1200\text{ cm}^{-1}$  and  $\sim 1500\text{ cm}^{-1}$ ). And the integrated area ratio of  $\text{sp}^3$ -type/ $\text{sp}^2$ -type carbon ( $A_{\text{sp}^3}/A_{\text{sp}^2}$ ) enables the evaluation of the relative contents of defective and graphitic carbon [57]. The  $I_{\text{D}}/I_{\text{G}}$  value, referring to the intensity ratio of the D-band to G-band, was approximately 1.30 and 1.08 for Fe1/2Zn-1.0CTAB and Fe1/2Zn-1.5CTAB, respectively, suggesting the formation of more lattice defects in the N-doped porous carbon matrices of Fe1/2Zn-1.0CTAB. In addition, the  $A_{\text{sp}^3}/A_{\text{sp}^2}$  value for Fe1/2Zn-1.0CTAB was as low as 0.38, which further demonstrates the high defective degree and outstanding electronic conductivity [58,59]. As reported, the catalysts with abundant defects are endowed with localized electrons, and the accelerated electron transfer facilitates the dissociation of  $\text{H}_2\text{O}_2$  to  $\cdot\text{OH}$  and Fe(III)/Fe(II) redox cycling [60–62].

The chemical states and local coordination environment of Fe atoms in Fe-SAC/NC were investigated by XANES and EXAFS. Fig. 3a displays the normalized Fe K-edge XANES spectra of the as-synthesized Fe-SAC/NC and the corresponding Fe foil, FeO and  $\text{Fe}_2\text{O}_3$  references. The increase in the valence of Fe would lead to the migration of the rising edge to higher energy region [23]. As can be seen, the near-edge absorption energy of the Fe K-edge for Fe-SAC/NC located between those of FeO and  $\text{Fe}_2\text{O}_3$ , indicating that the Fe atoms in the sample carried a positive charge with the oxidation value between +2 and +3. The Fourier transform extended X-ray absorption fine structure (FT-EXAFS) spectrum of Fe-SAC/NC in Fig. 3b exhibits a prominent peak at  $\sim 1.6\text{ \AA}$ ,

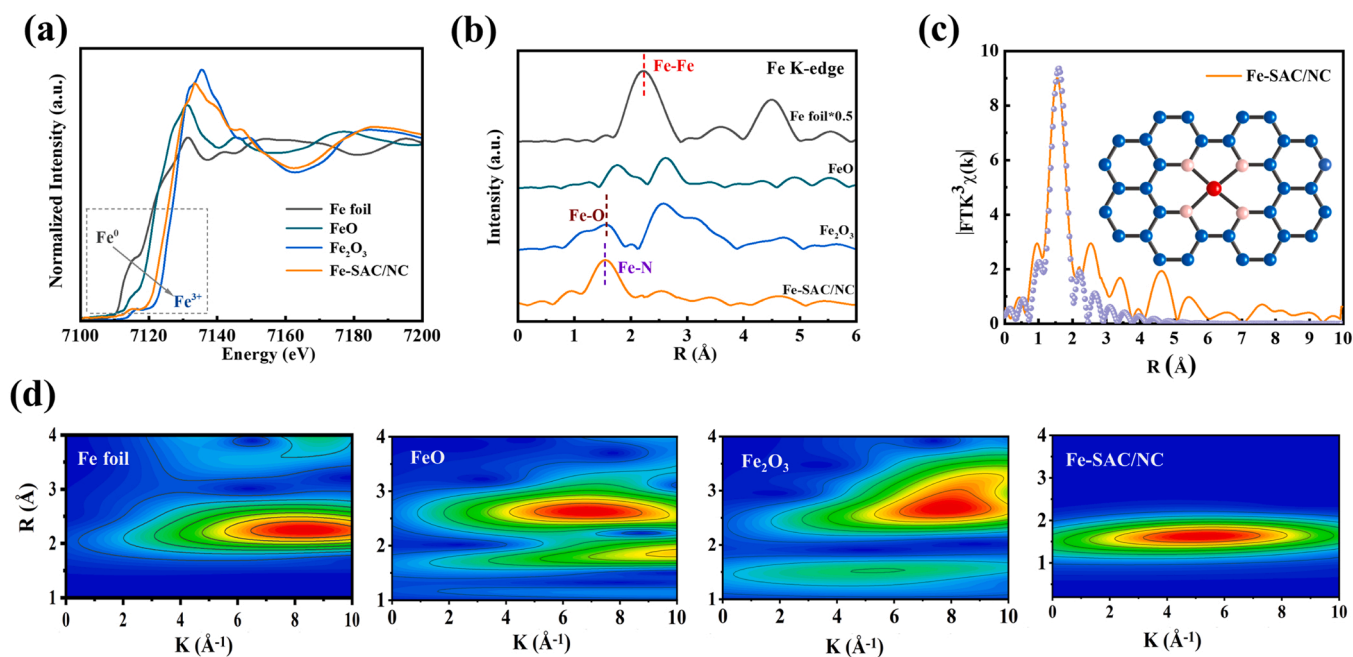


**Fig. 3.** (a) XANES curves and (b) FT-EXAFS curves at Fe K-edge obtained for Fe foil, FeO,  $\text{Fe}_2\text{O}_3$ , and Fe-SAC/NC. (c) Corresponding fitting for the FT-EXAFS curve of Fe-SAC/NC over the R space range (inset: model of  $\text{FeN}_4$  site in Fe-SAC/NC; the red, pink, and blue balls represent Fe, N and C, respectively). (d) Wavelet transform (WT) contour plots of Fe K-edge for Fe foil, FeO,  $\text{Fe}_2\text{O}_3$  and Fe-SAC/NC.



which can be assigned to Fe-N bonds [63]. The typical peak for Fe-Fe scattering path, located at  $\sim 2.4$  Å in the Fe foil, is absent in the spectrum of Fe-SAC/NC, providing solid evidence for the absence of metallic iron clusters or nanoparticles in the sample. The EXAFS fitting analysis further revealed the coordination environment of Fe in Fe-SAC/NC. The fitting results in Fig. 3c and Table S2 verified that each Fe atom was coordinated by 4 N atoms with the mean bond length of  $\sim 2.07$  Å. Moreover, the EXAFS wavelet transform (WT) plot of Fe-SAC/NC (Fig. 3d) only displayed an intensity maximum at 5.0 Å that is associated with the Fe-N coordination, being clearly distinguished from the Fe-Fe connection at 8.3 Å depicted in the plot of Fe foil. According to these results, it can be concluded that the Fe-SAC/NC with robust single-atom FeN<sub>4</sub> sites was successfully fabricated.

### 3.2. Evaluation of the catalytic activity of Fe-SAC/NC

To estimate the catalytic activity of the Fe-SAC/NC as a potential HEF catalyst, 2,4-dichlorophenol (2,4-DCP) was selected as the target contaminant to be treated by different processes (Fig. 4a). In electrochemical oxidation with in-situ generation of H<sub>2</sub>O<sub>2</sub> at the cathode (so-called EO-H<sub>2</sub>O<sub>2</sub>) [64], only a small 2,4-DCP removal of 17.3% in 90 min was achieved. The adsorption efficiency of 2,4-DCP by Fe-SAC/NC was also as low as 15.6%. These results suggest the negligible contribution of anodic oxidation and adsorption to 2,4-DCP removal. In contrast, complete abatement of 2,4-DCP was reached by Fe-SAC/NC-catalyzed HEF process in 90 min, with extremely low iron leaching (1.23 mg L<sup>-1</sup>), behaving much better than HEF with Fe-NP/NC catalyst that only allowed attaining a 40.9% removal. The remarkable catalytic activity and stability of the Fe-SAC/NC can be ascribed to the abundant accessible single-atom FeN<sub>4</sub> sites.

Since the chemical states and electronic features of the catalysts may vary under different synthesis conditions, the catalysts prepared with

different amount of CTAB source were tested in the HEF treatment of 2,4-DCP. As depicted in Fig. 4b, Fe1/2Zn-1.0CTAB exhibited the best activity in terms of 2,4-DCP degradation, attaining a 99.3% removal at 60 min, being superior to Fe1/2Zn-1.5CTAB (95.3%), Fe1/2Zn-0.5CTAB (60.9%) and Fe1/2Zn-0.1CTAB (47.1%). As described in Fig. S3, the proportion of different N species in the catalyst highly depended on the dosage of CTAB and, among them, Fe-N and pyrrolic N may play significant roles in the removal of 2,4-DCP. Therefore, the relationship between the kinetic constants for the degradation of 2,4-DCP and the relative contents of Fe-N and pyrrolic N in the catalysts can be inferred from data shown in Figs. 4c and 2e, respectively. The increase in the CTAB dose from 0.1 to 1.0 g led to growing percentages of Fe-N and pyrrolic N, which also yielded quicker 2,4-DCP disappearance. The results verify again the positive effect of Fe-N and pyrrolic N on the catalytic performance. However, further increase of the CTAB dosage to 1.5 g was detrimental, evidenced from the less effective 2,4-DCP abatement. This was due to the fact that excessive CTAB hinders the nucleation and growth of ZIF-8 precursor, then hampering the formation of single-atom FeN<sub>4</sub> sites despite the increase in the Fe-N content.

The effect of various operation parameters, including pH, catalyst dosage and applied current, on the 2,4-DCP concentration decay upon the application of Fe-SAC/NC-catalyzed HEF treatment was explored. As expected, increasing the catalyst dosage from 0.05 to 0.20 g L<sup>-1</sup> allowed the substantial enhancement of 2,4-DCP concentration decay (Fig. 4d). Notably, a dramatic increase in the 2,4-DCP removal was achieved when the catalyst dosage was increased from 0.05 to 0.10 g L<sup>-1</sup>, with only a small rise in iron leaching (i.e., 0.26 mg L<sup>-1</sup>, see inset), indicating that the greater catalytic performance was due to the increased amount of single-atom FeN<sub>4</sub> active sites rather than the homogeneous Fenton's reaction by the dissolved iron ions. As shown in Fig. 4e, the quickest decay of 2,4-DCP was observed at initial pH 3.0, and the degradation efficiency was gradually decreased with the increase in pH value. The

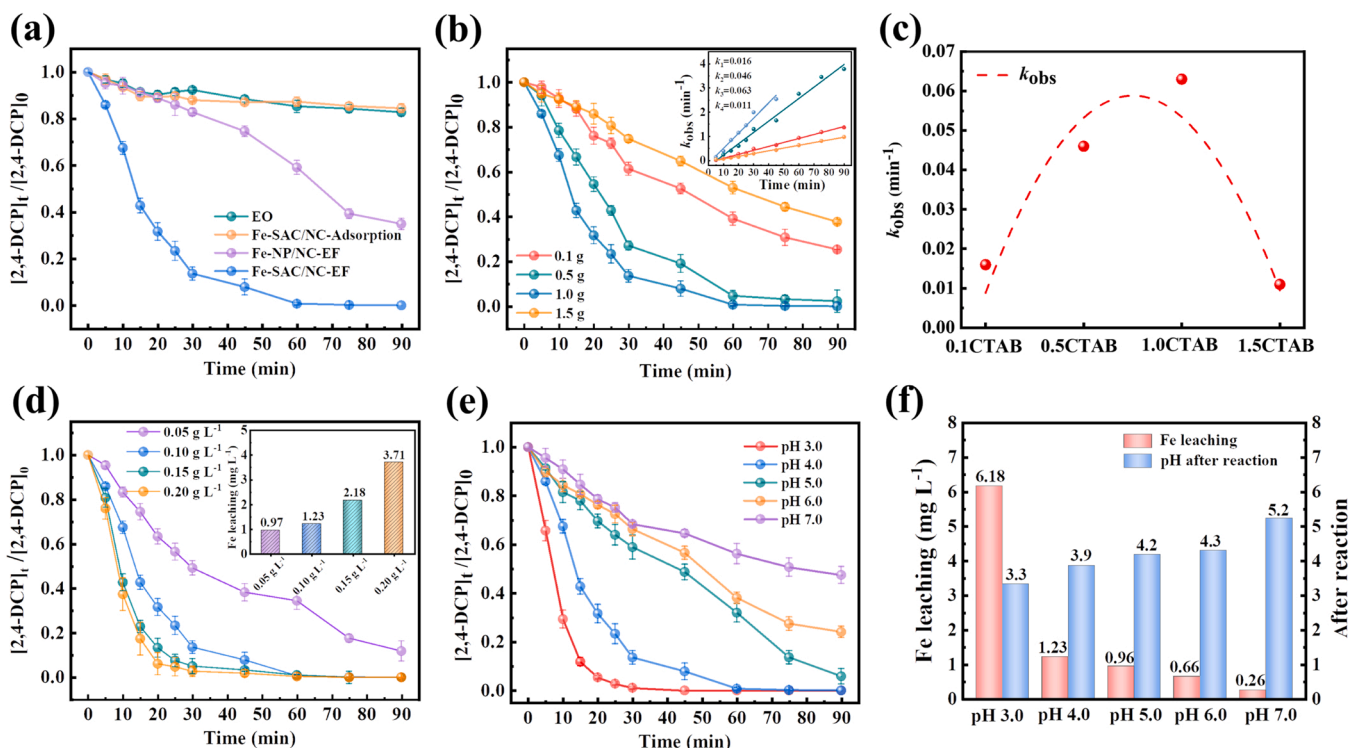


**Fig. 4.** (a) Normalized 2,4-DCP concentration decay during different treatments of 160 mL of 0.14 mM 2,4-DCP solutions with 0.05 M Na<sub>2</sub>SO<sub>4</sub>. (b) Effect of CTAB dosage, employed during the catalyst preparation, on the catalytic performance during the HEF treatment of 2,4-DCP solutions (inset: the corresponding kinetic analysis and pseudo-first-order rate constants). (c) Dependence of the rate constant values ( $k_{\text{obs}}$ ) for 2,4-DCP degradation (extracted from b). Effect of (d) catalyst dosage and (e) initial pH on the time course of normalized 2,4-DCP concentration during the Fe-SAC/NC-catalyzed HEF treatment (inset in (d): iron concentration after 90 min treatment). (f) Iron concentration and final pH after 90 min of the electrolytic trials shown in e.

enhanced performance at more acidic pH is logically attributed to the higher oxidation potential of  $\cdot\text{OH}$  at low pH, as well as the contribution of homogeneous Fenton's reaction occurring from dissolved iron ions (Fig. 4f). In other words, the loss of atomically dispersed iron sites at strong acidic pH would reduce the recyclability of Fe-SAC/NC. Fortunately, 100% and 96.8% 2,4-DCP removal could be still obtained at initial pH 4.0 and 5.0 with low iron leaching of 1.23 and 0.96  $\text{mg L}^{-1}$ , respectively, corroborating both the high activity and stability of the catalyst at near-neutral pH. Fig. S4 illustrates the positive effect of applied current increase on pollutant removal. The higher current gave rise to greater  $\text{H}_2\text{O}_2$  accumulation in the bulk and, consequently, to a higher amount of  $\cdot\text{OH}$ . The catalytic performance of Fe-SAC/NC-based HEF system was further investigated by treating several organic pollutants separately. As illustrated in Fig. 5a, the complete degradation of Rhodamine B, trimethylolpropane and ciprofloxacin and more than 90% removal of Methyl Orange can be observed in 30 min, whereas other pollutants were also completely removed in 60 min. Such results can be explained by the unique feature of  $\cdot\text{OH}$ , being nonselective in the degradation of most organics. Besides, the physicochemical properties of the organics, such as molecular structure and electron affinity, can affect their adsorption and decomposition, leading to different kinetic constants (Fig. 5a).

### 3.3. Recyclability and applicability of Fe-SAC/NC

Apart from the catalytic activity, the recyclability of the Fe-SAC/NC was also assessed from cycling tests. As depicted in Fig. 5b, the complete removal profiles of 2,4-DCP remained unaltered after five successive runs, demonstrating the remarkable recyclability of Fe-SAC/NC. The leached iron concentration was 1.23  $\text{mg L}^{-1}$  at the first cycle, then being undetectable after the second run. The slight decrease in the degradation kinetic constant, especially in the fourth and fifth runs, informs about

certain deactivation of catalyst due to the loss of  $\text{FeN}_4$  active sites and the adsorption of some organic intermediates on the surface during the long-term operation. The optimization of the cleaning procedure based on organic solvent and weak acid solution may increase its regeneration.

The applicability of Fe-SAC/NC in real cases was further evaluated by treating 2,4-DCP in urban wastewater at initial pH 4.0 (Fig. 5c). The almost total disappearance of 2,4-DCP at 90 min is evidenced, being the removal slower than that in simulated aqueous matrix due to the competition of other organics in wastewater for the  $\cdot\text{OH}$  [56]. Moreover, the mineralization ability of Fe-SAC/NC-catalyzed HEF process was assessed from TOC analysis. In Fig. 5d, it can be seen that the BDD/air-diffusion cell achieved a substantial mineralization of 67.6% at 300 min, outperforming that with a  $\text{RuO}_2$ -based DSA anode thanks to the production of physisorbed BDD( $\cdot\text{OH}$ ) [65]. Consequently, the Fe-SAC/NC-catalyzed HEF system owns an interesting recyclability and applicability.

### 3.4. Mechanistic insights

The electrochemical impedance spectroscopy (EIS) Nyquist plots were obtained to evaluate the ability of the Fe-SAC/NC to shuttle and conduct the surface charge (Fig. S5). The  $R_{ct}$  value (inset), which is related to the charge-transfer resistance of the catalyst, was acquired from the fitting of the corresponding equivalent circuit [66,67]. The results in Fig. S5 revealed that the  $R_{ct}$  values for Fe-SAC/CN and Fe-NP/CN were 3.44 and 7.10  $\text{k}\Omega$ , respectively, demonstrating the enhanced charge transfer efficiency of Fe-SAC/NC due to the addition of CTAB during the synthesis.

DFT calculations on the Gibbs free energy during  $\text{H}_2\text{O}_2$  adsorption and activation by the  $\text{FeN}_4$  or  $\text{Fe}_3\text{N}$  sites were carried out comparatively to provide insights into the catalytic mechanisms. The details are shown in Fig. 6a. The  $\text{H}_2\text{O}_2$  molecule is first adsorbed on top of the iron site

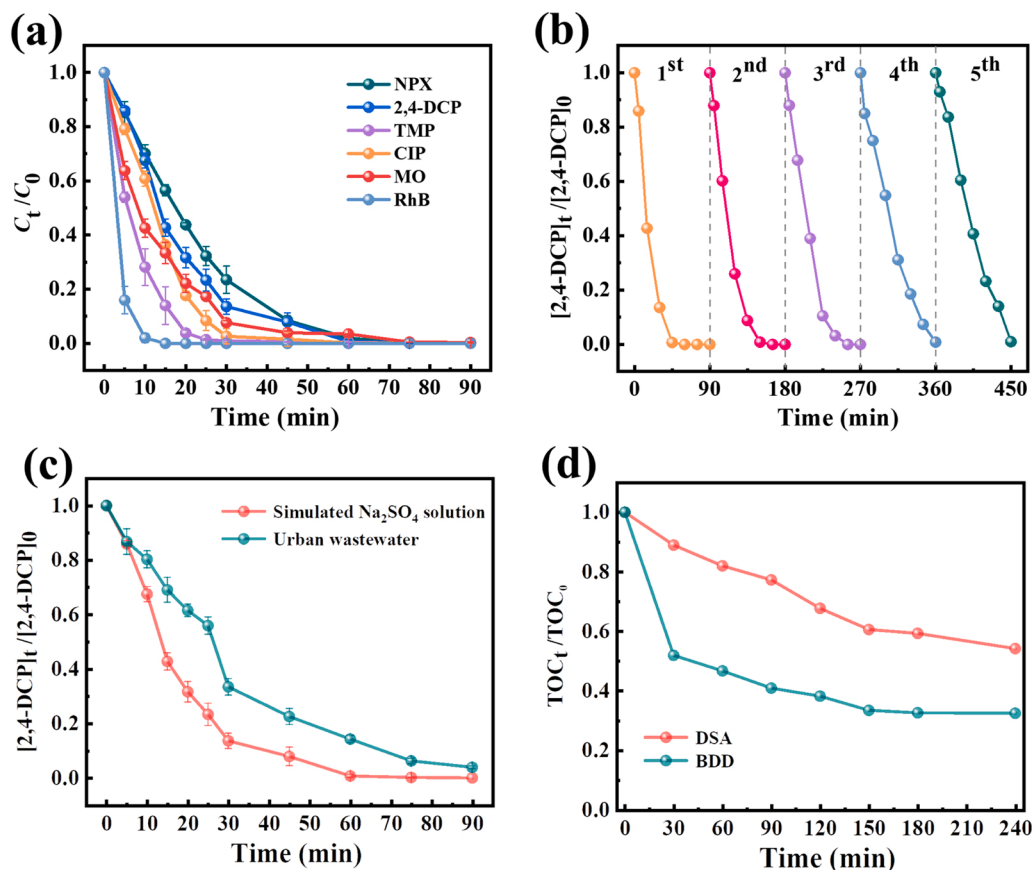


Fig. 5. (a) The degradation performance of Fe-SAC/NC-catalyzed HEF process considering different target organic pollutants, e.g., naproxen (NPX), 2,4-DCP, trimethylolpropane (TMP), ciprofloxacin (CIP), Methyl Orange (MO), and Rhodamine B (RhB). (b) Recycling of Fe-SAC/NC in the HEF treatment of 2,4-DCP solutions. (Unless otherwise stated, the parameters in each figure are: TOC of 10  $\text{mg L}^{-1}$ ; [Catalyst] = 0.10  $\text{g L}^{-1}$ ; initial pH = 4.0; applied current = 50 mA). (c) Degradation of 2,4-DCP in 160 mL of urban wastewater by Fe-SAC/NC-catalyzed HEF process at pH 4.0 and applied current of 50 mA. (d) Change of normalized TOC with reaction time during HEF treatment of 2,4-DCP solutions using a DSA or BDD anode under the conditions of the trial shown in Fig. 4a.

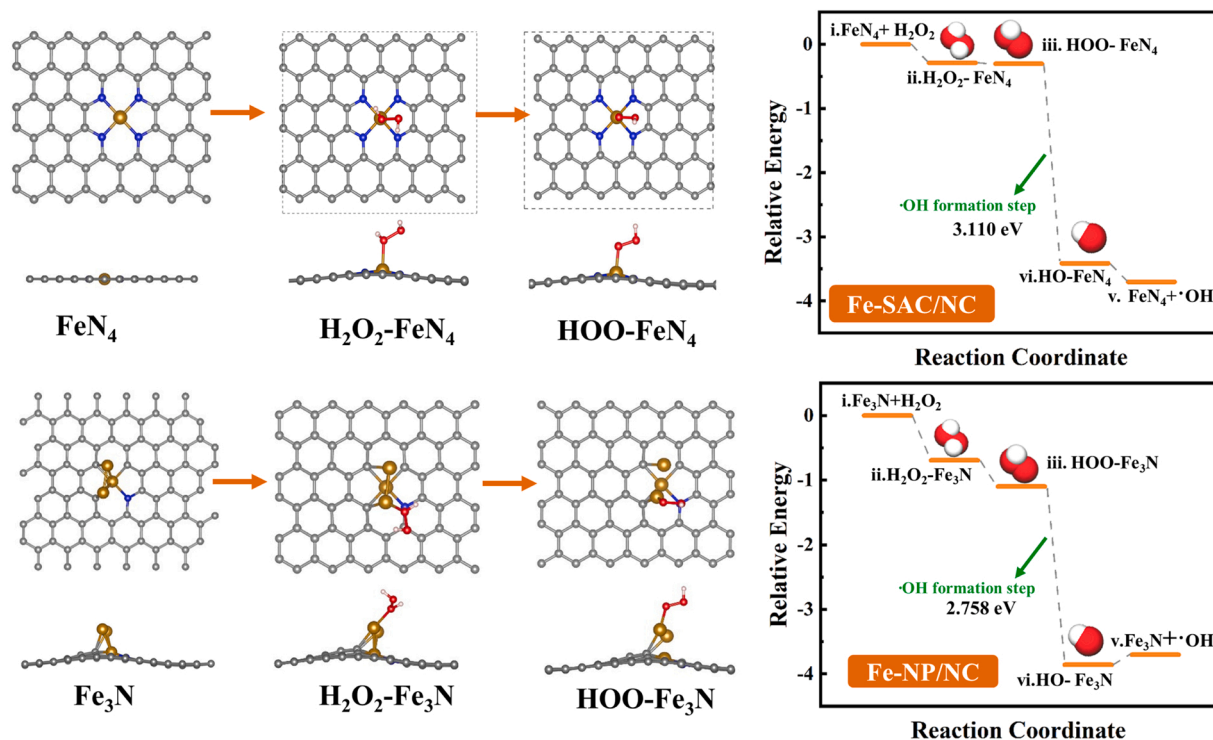


Fig. 6. Reaction pathways for  $\text{H}_2\text{O}_2$  adsorption and activation at  $\text{FeN}_4$  and  $\text{Fe}_3\text{N}$  sites, and required energy calculated by DFT.

( $\text{FeN}_4$  or  $\text{Fe}_3\text{N}$ ) with one of the O atoms bound to the iron atom ( $\text{H}_2\text{O}_2^*$ ). The  $\text{HOO-FeN}_4$  or  $\text{HOO-Fe}_3\text{N}$  bond ( $\text{HOO}^*$ ) is then achieved by releasing one proton. Finally, the O-O bond of the intermediate  $\text{HOO}^*$  is broken to yield the  $\text{HO}^*$  species, which can be desorbed from the catalyst quickly to degrade the organic molecules [59,68,69]. The superior catalytic activity of Fe-SAC/NC over Fe-NP/NC for HEF can be ascribed to two facts: (i) the desorption step to yield  $\bullet\text{OH}$  species in Fe-SAC/NC is an exothermal reaction and a feasible process, whereas the formation of the same oxidant from  $\text{HO-FeN}_4$  bond is an endothermal reaction (Fig. 6, right plot); (ii) the Gibbs free energy difference value of Fe-SAC/NC ( $\Delta G = -3.110$  eV) is greater than that of Fe-NP/NC ( $\Delta G = -2.758$  eV) during the breakage of  $\text{HOO}^*$  to  $\text{HO}^*$ , indicating the easier cleavage of

$\text{H}_2\text{O}_2$  to form  $\bullet\text{OH}$ . Such differences confirm the excellent activity of single-atom  $\text{FeN}_4$  sites towards  $\text{H}_2\text{O}_2$  activation, in full agreement with the previous experimental results.

Based on the above findings, a detailed mechanism explaining the superior performance of Fe-SAC/NC-catalyzed HEF treatment of 2,4-DCP (also valid for other organic pollutants) is proposed (Fig. 7). First, the in-situ generated  $\text{H}_2\text{O}_2$  at the cathode can be efficiently adsorbed at the  $\text{FeN}_4$  sites; then, it is rapidly decomposed to form a large number of  $\bullet\text{OH}$  via the interaction between  $\text{H}_2\text{O}_2$  and  $\text{FeN}_4$  sites. Meanwhile, the pyrrolic N in the catalyst favors the adsorption of the pollutant through the  $\pi$ - $\pi$  and/or cation- $\pi$  interactions. The enhanced mass transport decreases the migration distance between  $\bullet\text{OH}$  and target 2,4-DCP

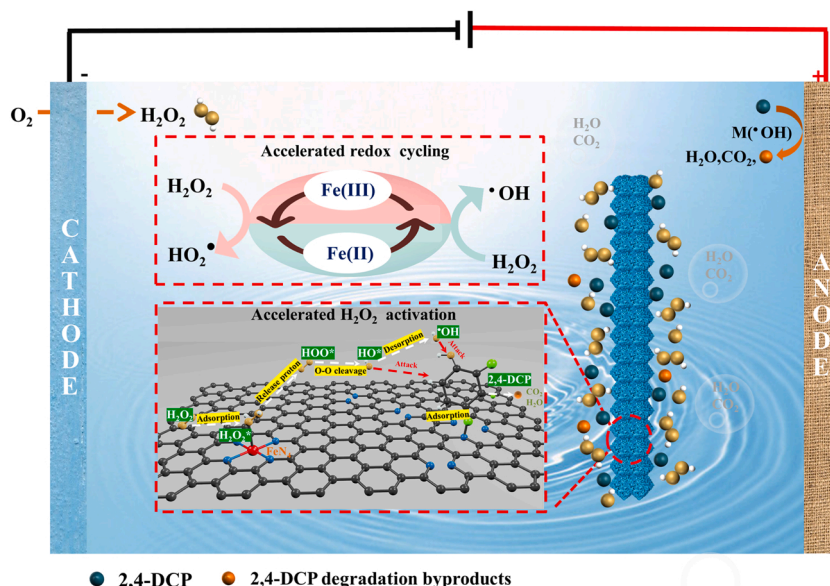


Fig. 7. Proposed mechanism for Fe-SAC/NC-catalyzed HEF degradation of 2,4-DCP.



molecules, resulting in the efficient degradation of the pollutant. As the reactions proceed, the single-atom FeN<sub>4</sub> sites undergo repetitive inter-conversion of the states during H<sub>2</sub>O<sub>2</sub> adsorption and activation, leading to excellent catalytic performance. On the other hand, the ultrathin carbon layer derived from CTAB not only suppresses the agglomeration of iron atoms, but also facilitates the formation of robust FeN<sub>4</sub> moieties during the synthesis. The coordination between Fe and N actually decreases the electron density of iron sites due to the high electronegativity of N element, which accelerates the Fe(III)/Fe(II) redox cycling during the treatment.

#### 4. Conclusions

Robust single-atom FeN<sub>4</sub> sites anchored on an N-doped carbon matrix were successfully prepared for the efficient HEF treatment of 2,4-DCP and other organic pollutants. Complete abatement of 2,4-DCP was attained by Fe-SAC/NC-catalyzed HEF process at 90 min, with very low iron leaching (1.23 mg L<sup>-1</sup>), which was superior to HEF with Fe-NP/NC catalyst that only allowed 41% 2,4-DCP removal. The Fe-SAC/NC exhibited reasonable stability and recyclability in HEF system. The dominant role of FeN<sub>4</sub> sites was verified from the thorough catalyst characterization and the experimental assays and DFT calculations. The modulation of the electronic structure of the catalyst by constructing dense FeN<sub>4</sub> moieties facilitated the electron transfer to yield a larger amount of <sup>•</sup>OH during the HEF, whereas the adjacent pyrrolic N enhanced the adsorption of target organic pollutants. These findings provide new insights into the rational design of highly active, stable, and multi-functional HEF catalysts, and inspire the exploration and application of electrochemical advanced oxidation technologies for real wastewater treatment.

#### CRedit authorship contribution statement

**Pan Xia:** Conceptualization, Data curation, Investigation, Validation. **Zhihong Ye:** Conceptualization, Funding acquisition, Investigation, Methodology, Project administration, Resources, Supervision, Writing – original draft. **Lele Zhao:** Investigation. **Qian Xue:** Investigation, Validation. **Sonia Lanzalaco:** Formal analysis, Validation, Writing – review & editing. **Qiang He:** Formal analysis. **Xueqiang Qi:** Investigation, Validation. **Ignasi Sirés:** Funding acquisition, Methodology, Project administration, Resources, Supervision, Writing – review & editing.

#### Declaration of Competing Interest

The authors declare that they have no known competing financial interests or personal relationships that could have appeared to influence the work reported in this paper.

#### Data availability

Data will be made available on request.

#### Acknowledgments

The authors gratefully acknowledge financial support from the National Natural Science Foundation of China (No. 52100073), the Fundamental Research Funds for the Central Universities (2021CDJQY-054, China), Venture and Innovation Support Program for Chongqing Overseas Returnees (cx2022048, China) and project PID2019-109291RB-I00 (MCIN/AEI/10.13039/501100011033, Spain). The Ph. D. scholarship awarded to L.Z. (State Scholarship Fund, CSC, China) is also acknowledged.

#### Appendix A. Supplementary material

Supplementary data associated with this article can be found in the online version at doi:10.1016/j.apcatb.2022.122116.

#### References

- [1] E. Mousset, Y. Pechaud, N. Oturan, M.A. Oturan, Charge transfer/mass transport competition in advanced hybrid electrocatalytic wastewater treatment: development of a new current efficiency relation, *Appl. Catal. B: Environ.* 240 (2019) 102–111, <https://doi.org/10.1016/j.apcatb.2018.08.055>.
- [2] V.H. Nguyen, S.M. Smith, K. Wantala, P. Kajitvichyanukul, Photocatalytic remediation of persistent organic pollutants (POPs): a review, *Arab. J. Chem.* 13 (2020) 8309–8337, <https://doi.org/10.1016/j.arabjc.2020.04.028>.
- [3] S.O. Ganiyu, C.A. Martínez-Huitle, M.A. Oturan, Electrochemical advanced oxidation processes for wastewater treatment: advances in formation and detection of reactive species and mechanisms, *Curr. Opin. Electrochem.* 27 (2021), 100678, <https://doi.org/10.1016/j.coelec.2020.100678>.
- [4] E. Brillas, Progress of homogeneous and heterogeneous electro-Fenton treatments of antibiotics in synthetic and real wastewaters: a critical review on the period 2017–2021, *Sci. Total Environ.* 819 (2022), 153102, <https://doi.org/10.1002/celc.202100588>.
- [5] N. Oturan, J. Bo, C. Trelu, M.A. Oturan, Comparative performance of ten electrodes in electro-Fenton process for removal of organic pollutants in water, *ChemElectroChem* 8 (2021) 3294–3303, <https://doi.org/10.1002/celc.202100588>.
- [6] I. Sirés, E. Brillas, Upgrading and expanding the electro-Fenton and related processes, *Curr. Opin. Electrochem.* 227 (2021), 100686, <https://doi.org/10.1016/j.coelec.2020.100686>.
- [7] H. Roth, Y. Gendel, P. Buzatu, O. David, M. Wessling, Tubular carbon nanotube-based gas diffusion electrode removes persistent organic pollutants by a cyclic adsorption-electro-Fenton process, *J. Hazard. Mater.* 307 (2016) 1–6, <https://doi.org/10.1016/j.jhazmat.2015.12.066>.
- [8] G. Daniel, Y. Zhang, S. Lanzalaco, F. Brombin, T. Kosmala, G. Granozzi, A. Wang, E. Brillas, I. Sirés, C. Durante, Chitosan-derived nitrogen-doped carbon electrocatalyst for a sustainable upgrade of oxygen reduction to hydrogen peroxide in UV-assisted electro-Fenton water treatment, *ACS Sustain. Chem. Eng.* 8 (2020) 14425–14440, <https://doi.org/10.1021/acssuschemeng.0c04294>.
- [9] Y. Zhang, G. Daniel, S. Lanzalaco, A.A. Isse, A. Facchin, A. Wang, E. Brillas, C. Durante, I. Sirés, H<sub>2</sub>O<sub>2</sub> production at gas-diffusion cathodes made from agarose-derived carbons with different textural properties for acetaminophen degradation in chloride media, *J. Hazard. Mater.* 423 (2022), 127005, <https://doi.org/10.1016/j.jhazmat.2021.127005>.
- [10] F.C. Moreira, R.A.R. Boaventura, E. Brillas, V.J.P. Vilar, Electrochemical advanced oxidation processes: a review on their application to synthetic and real wastewaters, *Appl. Catal. B: Environ.* 202 (2017) 217–261, <https://doi.org/10.1016/j.apcatb.2016.08.037>.
- [11] M. Pacheco-Álvarez, R.P. Benítez, O.M. Rodríguez-Narváez, E. Brillas, J.M. Peralta-Hernández, A critical review on paracetamol removal from different aqueous matrices by Fenton and Fenton-based processes, and their combined methods, *Chemosphere* 303 (2022), 134883, <https://doi.org/10.1016/j.chemosphere.2022.134883>.
- [12] S.O. Ganiyu, M. Zhou, C.A. Martínez-Huitle, Heterogeneous electro-Fenton and photoelectro-Fenton processes: a critical review of fundamental principles and application for water/wastewater treatment, *Appl. Catal. B: Environ.* 235 (2018) 103–129, <https://doi.org/10.1016/j.apcatb.2018.04.044>.
- [13] J. Hu, S. Wang, J. Yu, W. Nie, J. Sun, S. Wang, Duet Fe<sub>3</sub>C and FeN<sub>x</sub> sites for H<sub>2</sub>O<sub>2</sub> generation and activation toward enhanced electro-Fenton performance in wastewater treatment, *Environ. Sci. Technol.* 55 (2021) 1260–1269, <https://doi.org/10.1021/acs.est.0c06825>.
- [14] V. Poza-Nogueiras, E. Rosales, M. Pazos, M.A. Sanroman, Current advances and trends in electro-Fenton process using heterogeneous catalysts-A review, *Chemosphere* 201 (2018) 399–416, <https://doi.org/10.1016/j.chemosphere.2018.03.002>.
- [15] Z. Ye, G.E.M. Schukraft, A. L'Hermitte, Y. Xiong, E. Brillas, C. Petit, I. Sirés, Mechanism and stability of an Fe-based 2D MOF during the photoelectro-Fenton treatment of organic micropollutants under UVA and visible light irradiation, *Water Res.* 184 (2020), 115986, <https://doi.org/10.1016/j.watres.2020.115986>.
- [16] B. Singh, M.B. Gawande, A.D. Kute, R.S. Varma, P. Fornasiero, P. McNeice, R. V. Jagadeesh, R. Beller, R. Zboril, Single-atom (iron-based) catalysts: synthesis and applications, *Chem. Rev.* 121 (2021) 13620–13697, <https://doi.org/10.1021/acs.chemrev.1c00158>.
- [17] Y. Shang, X. Duan, S. Wang, Q. Yue, B. Gao, X. Xu, Carbon-based single atom catalyst: Synthesis, characterization, DFT calculations, *Chin. Chem. Lett.* 33 (2021) 663–673, <https://doi.org/10.1016/j.ccl.2021.07.050>.
- [18] H. Yu, Y. Xue, Y. Li, Graphdiyne and its assembly architectures: synthesis, functionalization, and applications, *Adv. Mater.* 31 (2019), 1803101, <https://doi.org/10.1002/adma.201803101>.
- [19] K. Tian, J. Wang, L. Cao, W. Yang, W. Guo, S. Liu, W. Li, F. Wang, X. Li, Z. Xu, Z. Wang, H. Wang, Y. Huo, Single-site pyrrolic-nitrogen-doped sp(2)-hybridized carbon materials and their pseudocapacitance, *Nat. Commun.* 11 (2020) 3884, <https://doi.org/10.1038/s41467-020-17727-y>.
- [20] W. Miao, Y. Liu, D. Wang, N. Du, Z. Ye, Y. Hou, S. Mao, K. Ostrikov, The role of Fe-N<sub>x</sub> single-atom catalytic sites in peroxymonosulfate activation: formation of



- surface-activated complex and non-radical pathways, *Chem. Eng. J.* 423 (2021), 130250, <https://doi.org/10.1016/j.cej.2021.130250>.
- [21] X. Xie, L. Peng, H. Yang, G.I.N. Waterhouse, L. Shang, T. Zhang, MIL-101-derived mesoporous carbon supporting highly exposed Fe single-atom sites as efficient oxygen reduction reaction catalysts, *Adv. Mater.* 33 (2021), 2101038, <https://doi.org/10.1002/adma.202101038>.
  - [22] L. Yu, Y. Li, Y. Ruan, Dynamic control of sacrificial bond transformation in the Fe-N-C single-atom catalyst for molecular oxygen reduction, *Angew. Chem. Int. Ed.* 60 (2021) 25296–25301, <https://doi.org/10.1002/ange.202111761>.
  - [23] X. Peng, J. Wu, Z. Zhao, X. Wang, H. Dai, L. Xu, G. Xu, Y. Jian, F. Hu, Activation of peroxymonosulfate by single-atom Fe-g-C<sub>3</sub>N<sub>4</sub> catalysts for high efficiency degradation of tetracycline via nonradical pathways: Role of high-valent iron-oxo species and Fe-N<sub>x</sub> sites, *Chem. Eng. J.* 427 (2022), 130803, <https://doi.org/10.1016/j.cej.2021.130803>.
  - [24] X. Li, X. Huang, S. Xi, S. Miao, J. Ding, W. Cai, S. Liu, X. Yang, H. Yang, J. Gao, J. Wang, Y. Huang, T. Zhang, B. Liu, Single cobalt atoms anchored on porous N-doped graphene with dual reaction sites for efficient Fenton-like catalysis, *J. Am. Chem. Soc.* 140 (2018) 12469–12475, <https://doi.org/10.1021/jacs.8b05992>.
  - [25] J. Yu, Z. Zhu, H. Zhang, Y. Qiu, D. Yin, Fe-nitrogen-doped carbon with dual active sites for efficient degradation of aromatic pollutants via peroxymonosulfate activation, *Chem. Eng. J.* 427 (2022), 130898, <https://doi.org/10.1016/j.cej.2021.130898>.
  - [26] Y. Li, X. Liu, L. Zheng, J. Shang, X. Wan, R. Hu, X. Guo, S. Hong, J. Shui, Preparation of Fe-N-C catalysts with FeN<sub>x</sub> (x = 1, 3, 4) active sites and comparison of their activities for the oxygen reduction reaction and performances in proton exchange membrane fuel cells, *J. Mater. Chem. A* 7 (2019) 26147–26153, <https://doi.org/10.1039/C9TA08532G>.
  - [27] I.S. Pieta, R.G. Kadam, P. Pieta, D. Mrdenovic, R. Nowakowski, A. Bakandritsos, M. Petr, M. Otyepka, R. Kostecki, M.A.M. Khan, R. Zboril, M.B. Gawande, The hallmarks of copper single atom catalysts in direct alcohol fuel cells and electrochemical CO<sub>2</sub> fixation, *Adv. Mater. Interfaces* 8 (2021), 2001822, <https://doi.org/10.1002/admi.202001822>.
  - [28] R.G. Kadam, T. Zhang, D. Zaoralová, M. Medved, A. Bakandritsos, O. Tomanec, M. Petr, J.Z. Chen, J.T. Miller, M. Otyepka, R. Zboril, T. Asefa, M.B. Gawande, Single Co-atoms as electrocatalysts for efficient hydrazine oxidation reaction, *Small* 17 (2021), 2006477, <https://doi.org/10.1002/smll.202006477>.
  - [29] P. Sharma, S. Kumar, O. Tomanec, M. Petr, J.Z. Chen, J.T. Miller, R.S. Varma, M. B. Gawande, R. Zboril, Carbon nitride-based ruthenium single atom photocatalyst for CO<sub>2</sub> reduction to methanol, *Small* 17 (2021), 2006478, <https://doi.org/10.1002/smll.202006478>.
  - [30] F. Chen, L. Liu, J. Wu, X. Rui, J. Chen, Y. Yu, Single-atom iron anchored tubular g-C<sub>3</sub>N<sub>4</sub> catalysts for ultrafast Fenton-like reaction: roles of high-valency iron-oxo species and organic radicals, *Adv. Mater.* 34 (2022), 2202891, <https://doi.org/10.1002/adma.202202891>.
  - [31] Y. Xiong, H. Li, C. Liu, L. Zheng, C. Liu, J. Wang, S. Liu, Y. Han, L. Gu, J. Qian, D. Wang, Single-atom Fe catalysts for Fenton-like reactions: roles of different N species, *Adv. Mater.* 34 (2022), 2110653, <https://doi.org/10.1002/adma.202110653>.
  - [32] P. Cao, X. Quan, K. Zhao, S. Chen, H. Yu, Y. Su, High-efficiency electrocatalysis of molecular oxygen toward hydroxyl radicals enabled by an atomically dispersed iron catalyst, *Environ. Sci. Technol.* 54 (2020) 12662–12672, <https://doi.org/10.1021/acs.est.0c03614>.
  - [33] K. Zhao, X. Quan, Y. Su, X. Qin, S. Chen, H. Yu, Enhanced chlorinated pollutant degradation by the synergistic effect between dechlorination and hydroxyl radical oxidation on a bimetallic single-atom catalyst, *Environ. Sci. Technol.* 55 (2021) 14194–14203, <https://doi.org/10.1021/acs.est.1c04943>.
  - [34] D. Zhang, K. Yin, Y. Tang, Y. Wei, H. Tang, H. Liu, Y. Chen, C. Liu, Hollow sear-urchin-shaped carbon-anchored single-atom iron as dual-functional electro-Fenton catalysts for degrading refractory thiamphenicol with fast reaction kinetics in a wide pH range, *Chem. Eng. J.* 427 (2022), 130996, <https://doi.org/10.1016/j.cej.2021.130996>.
  - [35] M. Liu, J. Lee, T. Yang, F. Zheng, J. Zhao, C. Yang, L.Y.S. Lee, Synergies of Fe single atoms and clusters on N-doped carbon electrocatalyst for pH-universal oxygen reduction, *Small Methods* 5 (2021), 001165, <https://doi.org/10.1002/smt.202001165>.
  - [36] L. Peng, X. Duan, Y. Shang, B. Gao, X. Xu, Engineered carbon supported single iron atom sites and iron clusters from Fe-rich enteromorpha for Fenton-like reactions via nonradical pathways, *Appl. Catal. B: Environ.* 287 (2021), 119963, <https://doi.org/10.1016/j.apcatb.2021.119963>.
  - [37] T.A. Goetjen, J. Liu, Y. Wu, J. Sui, X. Zhang, J.T. Hupp, O.K. Farha, Metal-organic framework (MOF) materials as polymerization catalysts: a review and recent advance, *Chem. Commun.* 56 (2020) 10409–10418, <https://doi.org/10.1039/DOCC03790G>.
  - [38] K. Dashtian, S. Shahbazi, M. Tayebi, Z. Masoumi, A review on metal-organic frameworks photoelectrochemistry: a headlight for future applications, *Coord. Chem. Rev.* 445 (2021), 214097, <https://doi.org/10.1016/j.ccr.2021.214097>.
  - [39] A. Han, B. Wang, A. Kumar, Y. Qin, J. Jin, X. Wang, C. Yang, B. Dong, Y. Jia, J. Liu, X. Sun, Recent advances for MOF-derived carbon-supported single-atom catalysts, *Small Methods* 3 (2019), 1800471, <https://doi.org/10.1002/smt.201800471>.
  - [40] Z. Song, L. Zhang, K. Doyle-Davis, F. Fu, J. Luo, X. Sun, Recent advances in MOF-derived single atom catalysts for electro recent advances for MOF-derived carbon-supported single-atom catalysts chemical applications, *Adv. Energy Mater.* 10 (2020), 2001561, <https://doi.org/10.1002/aenm.202001561>.
  - [41] Y. Wei, M. Zhang, R. Zou, Q. Xu, Metal-organic framework-based catalysts with single metal sites, *Chem. Rev.* 120 (2020) 12089–12174, <https://doi.org/10.1021/acs.chemrev.9b00757>.
  - [42] X. Chen, N. Wang, K. Shen, Y. Xie, Y. Tan, Y. Li, MOF-derived isolated Fe atoms implanted in N-doped 3D hierarchical carbon as an efficient ORR electrocatalyst in both alkaline and acidic media, *ACS Appl. Mater. Interfaces* 11 (2019) 25976–25985, <https://doi.org/10.1021/acsami.9b07436>.
  - [43] Y. He, S. Hwang, D.A. Cullen, M.A. Uddin, L. Langhorst, B. Li, S. Karakalos, A. J. Kropf, E.C. Wegener, J. Sokolowski, Highly active atomically dispersed CoN<sub>4</sub> fuel cell cathode catalysts derived from surfactant-assisted MOFs: carbon-shell confinement strategy, *Energy Environ. Sci.* 12 (2019) 250–260, <https://doi.org/10.1039/C8EE02694G>.
  - [44] X. Wang, C. Yang, X. Wang, H. Zhu, L. Cao, A. Chen, L. Gu, Q. Zhang, L. Zheng, H. Liang, Green synthesis of a highly efficient and stable single-atom iron catalyst anchored on nitrogen-doped carbon nanorods for the oxygen reduction reaction, *ACS Sustain. Chem. Eng.* 9 (2020) 137–146, <https://doi.org/10.1021/acssuschemeng.0c05509>.
  - [45] L. Zhou, P. Zhou, Y. Zhang, B. Liu, P. Gao, S. Guo, 3D star-like atypical hybrid MOF derived single-atom catalyst boosts oxygen reduction catalysis, *J. Energy Chem.* 55 (2021) 355–360, <https://doi.org/10.1016/j.jechem.2020.06.059>.
  - [46] J. Xiao, J. Chen, Z. Ou, J. Lai, T. Yu, Y. Wang, N-doped carbon-coated Fe<sub>3</sub>N composite as heterogeneous electro-Fenton catalyst for efficient degradation of organics, *Chin. J. Catal.* 42 (2021) 953–962, [https://doi.org/10.1016/S1872-2067\(20\)63719-6](https://doi.org/10.1016/S1872-2067(20)63719-6).
  - [47] X. Du, W. Fu, P. Su, L. Su, Q. Zhang, J. Cai, M. Zhou, Trace FeCu@PC derived from MOFs for ultraefficient heterogeneous electro-Fenton process: enhanced electron transfer and bimetallic synergy, *ACS ES&T Eng.* 1 (2021) 1311–1322, <https://doi.org/10.1021/acsestengg.1c00131>.
  - [48] Y. Gao, X. Duan, B. Li, Q. Jia, Y. Li, X. Fan, F. Zhang, G. Zhang, S. Wang, W. Peng, Fe containing templates derived atomic Fe-NC to boost Fenton-like reaction and the charge migration analysis on highly active Fe-N<sub>4</sub> sites, *J. Mater. Chem. A* 9 (2021) 14793–14805, <https://doi.org/10.1039/D1TA02446A>.
  - [49] Y. Li, X. Wei, L. Chen, J. Shi, M. He, Nickel-molybdenum nitride nanoplate electrocatalysts for concurrent electrolytic hydrogen and formate productions, *Nat. Commun.* 10 (2019) 1–12, <https://doi.org/10.1038/s41467-019-13375-z>.
  - [50] T. Yang, D. Yu, D. Wang, T. Yang, Z. Li, M. Wu, M. Petru, J. Crittenden, Accelerating Fe(III)/Fe(II) cycle via Fe(II) substitution for enhancing Fenton-like performance of Fe-MOFs, *Appl. Catal. B: Environ.* 286 (2021), 119859, <https://doi.org/10.1016/j.apcatb.2020.119859>.
  - [51] K. Yuan, S. Sfaelou, M. Qiu, D. Lützenkirchen-Hecht, X. Zhuang, Y. Chen, C. Yuan, X. Feng, U. Scherf, Synergetic contribution of boron and Fe-N<sub>x</sub> species in porous carbons toward efficient electrocatalysts for oxygen reduction reaction, *ACS Energy Lett.* 3 (2017) 252–260, <https://doi.org/10.1021/acsenrgylett.7b01188>.
  - [52] J. Han, X. Meng, L. Lu, J. Bian, Z. Li, C. Sun, Single-atom Fe-N<sub>x</sub>-C as an efficient electrocatalyst for zinc-air batteries, *Adv. Funct. Mater.* 29 (2019), 1808872, <https://doi.org/10.1002/adfm.201808872>.
  - [53] T. Yang, S. Fan, Y. Li, Q. Zhou, Fe-N/C single-atom catalysts with high density of Fe-N<sub>x</sub> sites toward peroxymonosulfate activation for high-efficient oxidation of bisphenol A: electron-transfer mechanism, *Chem. Eng. J.* 419 (2021), 129590, <https://doi.org/10.1016/j.cej.2021.129590>.
  - [54] S. Ren, X. Duan, M. Lei, S. Liang, M. Zhang, H. Zheng, Energetic MOF-derived cobalt/iron nitrides embedded into N,S-codoped carbon nanotubes as superior bifunctional oxygen catalysts for Zn-air batteries, *Appl. Surf. Sci.* 569 (2021), 151030, <https://doi.org/10.1016/j.apsusc.2021.151030>.
  - [55] J. Yang, D. Zeng, Q. Zhang, R. Cui, M. Hassan, L. Dong, J. Li, Y. He, Single Mn atom anchored on N-doped porous carbon as highly efficient Fenton-like catalyst for the degradation of organic contaminants, *Appl. Catal. B: Environ.* 279 (2020), 119363, <https://doi.org/10.1016/j.apcatb.2020.119363>.
  - [56] J. Yang, D. Zeng, J. Li, L. Dong, W. Ong, Y. He, A highly efficient Fenton-like catalyst based on isolated diatomic Fe-Co anchored on N-doped porous carbon, *Chem. Eng. J.* 404 (2021), 126376, <https://doi.org/10.1016/j.cej.2020.126376>.
  - [57] Z. Zhu, F. Cheng, J. Chen, Investigation of effects of carbon coating on the electrochemical performance of Li<sub>4</sub>Ti<sub>5</sub>O<sub>12</sub>/C nanocomposites, *J. Mater. Chem. A* 1 (2013) 9484–9490, <https://doi.org/10.1039/C3TA000114H>.
  - [58] W. Duan, Z. Hu, K. Zhang, F. Cheng, Z. Tao, J. Chen, Li<sub>3</sub>V<sub>2</sub>(PO<sub>4</sub>)<sub>3</sub>@C core-shell nanocomposite as a superior cathode material for lithium-ion batteries, *Nanoscale* 5 (2013) 6485–6490, <https://doi.org/10.1039/C3NR01617J>.
  - [59] F. Wang, N. Zhang, X. Zhao, L. Wang, J. Zhang, T. Wang, F. Liu, Y. Liu, L. Fan, Realizing a high-performance Na-storage cathode by tailoring ultrasmall Na<sub>2</sub>FePO<sub>4</sub>F nanoparticles with facilitated reaction kinetics, *Adv. Sci.* 6 (2019), 1900649, <https://doi.org/10.1002/advs.201900649>.
  - [60] L. Zhou, Q. Chang, C. Xue, N. Li, C. Hao, J. Yang, S. Hu, Graphitic carbon nitride modified with trace-level copper and carbon dots exhibits excellent photo-Fenton catalytic activity with low consumption of H<sub>2</sub>O<sub>2</sub>, *Ceram. Int.* 48 (2022) 17960–17968, <https://doi.org/10.1016/j.ceramint.2022.04.126>.
  - [61] H. Qi, X. Sun, Z. Sun, Porous graphite felt electrode with catalytic defects for enhanced degradation of pollutants by electro-Fenton process, *Chem. Eng. J.* 403 (2021), 126270, <https://doi.org/10.1016/j.cej.2020.126270>.
  - [62] Z. Wang, L. Pi, J. Cui, X. Zhang, Y. Liu, D. Tang, H. Zhu, X. Mao, Heterogeneous electro-Fenton system for efficient degradation of 2,4-DCP: dual activation of O<sub>2</sub> for H<sub>2</sub>O<sub>2</sub> generation and oxygen-defect cobalt ferrite catalyst, *Sep. Purif. Technol.* 255 (2021), 117731, <https://doi.org/10.1016/j.seppur.2020.117731>.
  - [63] K. Qian, H. Chen, W. Li, Z. Ao, Y. Wu, X. Guan, Single-atom Fe catalyst outperforms its homogeneous counterpart for activating peroxymonosulfate to achieve effective degradation of organic contaminants, *Environ. Sci. Technol.* 55 (2021) 7034–7043, <https://doi.org/10.1021/acs.est.0c08805>.
  - [64] S. Lanzaalaco, I. Sirés, M.A. Sabatino, C. Dispenza, O. Scialdone, A. Galia, Synthesis of polymer nanogels by electro-Fenton process: investigation of the effect of main

- operation parameters, *Electrochim. Acta* 246 (2017) 812–822, <https://doi.org/10.1016/j.electacta.2017.06.097>.
- [65] Z. Ye, J.A. Padilla, E. Xuriguera, E. Brillas, I. Sirés, Magnetic MIL(Fe)-type MOF-derived N-doped nano-ZVI@C rods as heterogeneous catalyst for the electro-Fenton degradation of gemfibrozil in a complex aqueous matrix, *Appl. Catal. B: Environ.* 266 (2020), 118604, <https://doi.org/10.1016/j.apcatb.2020.118604>.
- [66] W. Ren, D. Tang, X. Sun Lu, J. Li, M. Qiu, S. Fan, Novel multilayer ACF@rGO@OMC cathode composite with enhanced activity for electro-Fenton degradation of phthalic acid esters, *Ind. Eng. Chem. Res.* 55 (2016) 11085–11096, <https://doi.org/10.1021/acs.iecr.6b02896>.
- [67] Y. Li, N. Luo, Z. Tian, H. Li, M. Yang, W. Shang, Y. Shen, M. Qu, A. Zhou, H<sub>2</sub>O<sub>2</sub>-free photo-Fenton degradation of organic pollutants on thermally exfoliated g-C<sub>3</sub>N<sub>4</sub>, *Colloid Surf. A* 586 (2020), 124190, <https://doi.org/10.1016/j.colsurfa.2019.124190>.
- [68] Z. Guo, Y. Xie, J. Xiao, Z. Zhao, Y. Wang, Z. Xu, Y. Zhang, L. Yin, H. Cao, J. Gong, Single-atom Mn-N<sub>4</sub> site-catalyzed peroxone reaction for the efficient production of hydroxyl radicals in an acidic solution, *J. Am. Chem. Soc.* 141 (2019) 12005–12010, <https://doi.org/10.1021/jacs.9b04569>.
- [69] W. Xu, W. Xue, H. Huang, J. Wang, C. Zhong, D. Mei, Morphology controlled synthesis of  $\alpha$ -Fe<sub>2</sub>O<sub>3</sub>-x with benzimidazole-modified Fe-MOFs for enhanced photo-Fenton-like catalysis, *Appl. Catal. B: Environ.* 291 (2021), 120129, <https://doi.org/10.1016/j.apcatb.2021.120129>.